
Article:
Galetto, F, Hooper, A orcid.org/0000-0003-4244-6652, Bagnardi, M et al. (1 more author) (2020) The 2008 Eruptive Unrest at Cerro Azul Volcano (Galápagos) Revealed by InSAR Data and a Novel Method for Geodetic Modelling. Journal of Geophysical Research: Solid Earth, 125 (2). e2019JB018521. ISSN 2169-9313

https://doi.org/10.1029/2019jb018521

JGR Solid Earth

RESEARCH ARTICLE
10.1029/2019JB018521

Key Points:
- The 2008 eruptive unrest at Cerro Azul (Galápagos) was associated to the propagation of a radial dike
- To avoid unwrapping errors, we applied a new method for the inversion of InSAR data, based on wrapped phase differences
- The continuous supply of magma from the reservoir to the dike promoted the further propagation of the dike

Supporting Information:
- Supporting Information S1

Correspondence to:
F. Galetto,
federico.galetto@uniroma3.it

Citation:
Galetto, F., Hooper, A., Bagnardi, M., & Acocella, V. (2020). The 2008 eruptive unrest at Cerro Azul volcano (Galápagos) revealed by InSAR data and a novel method for geodetic modelling. *Journal of Geophysical Research: Solid Earth*, *125*, e2019JB018521. https://doi.org/10.1029/2019JB018521

Received 8 AUG 2019
Accepted 29 DEC 2019
Accepted article online 3 JAN 2020

The 2008 Eruptive Unrest at Cerro Azul Volcano (Galápagos) Revealed by InSAR Data and a Novel Method for Geodetic Modelling

Federico Galetto[1], Andrew Hooper[2], Marco Bagnardi[2,3], and Valerio Acocella[1]

[1]Università degli Studi di Roma Tre, Dipartimento di Scienze, Rome, Italy, [2]COMET, School of Earth and Environment, University of Leeds, Leeds, UK, [3]Now at NASA Goddard Space Flight Center, Greenbelt, MD, USA

Abstract Cerro Azul is one of the most active volcanoes in the western Galápagos Islands, but its unrest episodes are poorly studied. Unrest, which started in 2007, culminated in two eruptive phases from 29 May to 11 June 2008. We investigate this unrest and the associated eruptions using interferometric synthetic aperture radar (InSAR) data and geodetic modelling. To overcome the unwrapping errors affecting some of our InSAR data, we invert the wrapped phase directly by estimating the integer ambiguities simultaneously with the geophysical parameters. Our results highlight how the eruption was preceded by long-term pre-eruptive inflation (October 2007–April 2008). During the first eruptive phase, most of the magma responsible for the inflation fed the lateral propagation of a radial dike, which caused a first deflation of the magmatic reservoir. During the second eruptive phase, the further lateral propagation of the dike fed a radial eruptive fissure at the base of the edifice, causing further deflation of the magmatic reservoir. From the first to the second eruptive phase, the radial dike changed its strike propagating toward a topographic low between Cerro Azul and Sierra Negra.

1. Introduction

Basaltic shield volcanoes with summit calderas usually experience repeated unrest, during which the baseline of the monitoring parameters (e.g., degassing, seismicity, and ground deformation) deviates from quiescence (Acocella et al., 2015; Newhall & Dzurisin, 1988). Unrest episodes have important volcanic hazard implications, as nearly all eruptions are preceded by unrest episodes, although not all unrest necessarily culminates in eruption (Acocella et al., 2015; Biggs et al., 2014; Sandri et al., 2017). Understanding the nature and possible outcome of unrest becomes, therefore, crucial for the mitigation of volcanic risk. Adequate ground-based monitoring is often limited by the fact that many volcanic systems lie in remote areas, hindering the study of many unrest episodes. Volcano monitoring through remote sensing techniques, such as interferometric synthetic aperture radar interferometry (InSAR) can, on the other hand, overcome these limitations and allow investigations of unrest globally (Gaddes et al., 2019; Pinel et al., 2014). InSAR has proven to be successful at different volcanic provinces worldwide (e.g., Amelung et al., 2007; Baker & Amelung, 2012; Biggs et al., 2016; Ebmeier et al., 2013; González et al., 2015; Poland et al., 2017; Sigmundsson et al., 2015; Wright et al., 2006). Among these, the western Galápagos calderas have been extensively studied using InSAR data, improving our knowledge on these volcanoes and shallow magma transfer mechanisms (Bagnardi et al., 2013; Chadwick et al., 2011; Galetto et al., 2019; Jónsson, 2009; Xu et al., 2016). Here we investigate the 2007–2008 unrest of Cerro Azul volcano (western Galápagos), which culminated in two eruptive phases, from 29 May to 11 June 2008, using InSAR data and geodetic modelling. To avoid unwrapping errors due to erroneous estimation of the phase integer ambiguities during the so-called unwrapping process (e.g., Hooper & Zebker, 2007), which would bias InSAR data inversion results, we propose a method to model the wrapped data directly, instead of trying to solve them. This differs to the approach of Yun et al. (2007), who used amplitude offset estimates to first reduce the signal prior to unwrapping. We adopt our new method to interpret data from the ENVISAT satellite that are clearly affected by unwrapping errors. Results highlight how most of the deformation is related to the propagation of a radial dike, which triggered the two eruptive phases.

2. Geological Background

The Galápagos Archipelago, in the eastern Pacific Ocean, is a hot spot magmatic province. The islands lie above a broad and thick platform over young (<10 Ma) oceanic lithosphere (Figure 1a) (Feighner &

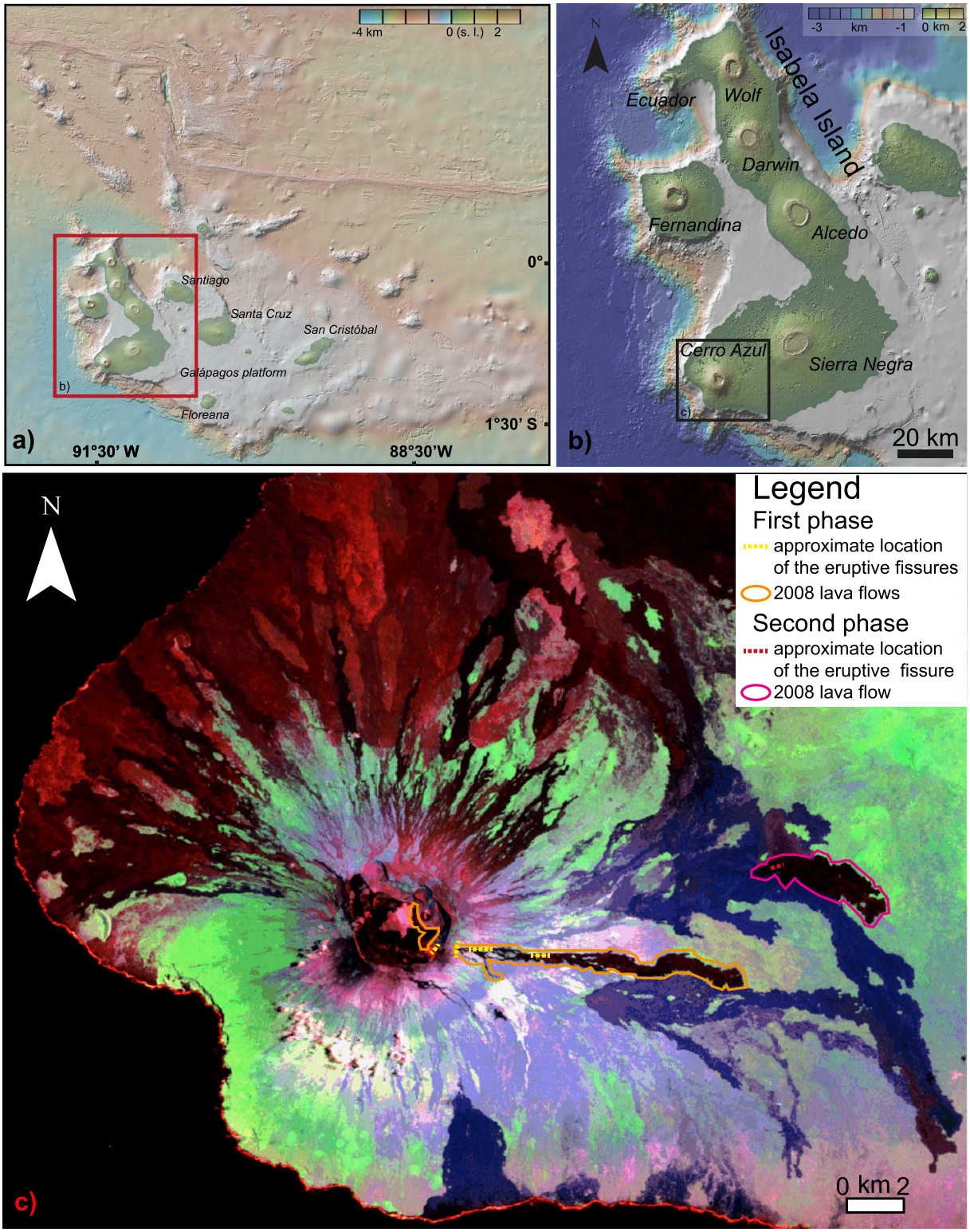

Figure 1. (a) Galápagos Archipelago. The red square outlines the extent of Panel b. (b) The western Galápagos Islands of Fernandina and Isabela, on which lies the volcano of Cerro Azul (the black square is the area in Panel c). Digital elevation model and bathymetry in (a) and (b) from GeoMappApp. (c) Filtered false colors (R = Band 2; G = Band 4; B = Band 5) Landsat 7 image of Cerro Azul acquired on 22 March 2009, showing the lava flows erupted in 2008. Dotted lines represent the approximate location of the eruptive fissures.

Richards, 1994; Rychert et al., 2014). Most of the current volcanic activity focuses on the seven shield volcanoes forming the western Galápagos Islands of Fernandina and Isabela, in the upwelling region of the hot spot (Gibson & Geist, 2010; Hooft et al., 2003; Villagómez et al., 2014). These volcanoes are large, flexurally supported shields with summit calderas, forming a distinct volcanological, petrological, geochemical, and structural group with respect to the eastern Galápagos volcanoes (Feighner & Richards, 1994; Harpp & Geist, 2018; White et al., 1993). Among the western Galápagos volcanoes is Cerro Azul, one of the six making up Isabela Island (Naumann & Geist, 2000). Cerro Azul has a maximum elevation of 1,640 m above sea level, with gently sloping lower flanks (generally <4°), steep upper flanks (generally ~25°), and a flat summit rim (~1 km wide) that surrounds a 450-m-deep nested caldera (Naumann & Geist, 2000). This 4.2 × 2.2 km wide caldera, with major axis oriented NW-SE, results from repeated cycles of collapse and is the smallest, both in volume (3.1 km^3) and area (9.5 km^2), among those of the western Galápagos (Naumann & Geist, 2000).

Cerro Azul has erupted some of the most primitive magmas of the western Galápagos and is the only western Galápagos volcano to have erupted both tholeiitic and alkali basalts (Naumann et al., 2002; Naumann & Geist, 1999). These characteristics have been related to its juvenile stage and relatively low magma supply rates (Naumann et al., 2002; Naumann & Geist, 1999). As a result, Cerro Azul is inferred to lack a well-developed shallow magmatic system, with probably only a hot and partially developed deep mushy system at 5 km below sea level (Geist et al., 2014: Harpp & Geist, 2018). A series of north- to northwest-trending landslide scarps suggests the collapse of the southwestern flank (Naumann & Geist, 2000). The failure of this flank, due to its position adjacent to the steep submarine escarpment (3 km height) (Figure 1b) (Geist et al., 2008), promotes the formation of northwest-southeast oriented eruptive fissures (Naumann et al., 2002; Naumann & Geist, 2000).

More in general, Cerro Azul shows the typical eruptive pattern of the western Galápagos volcanoes, with circumferential eruptive fissures just outside the caldera rim and radial fissures along the volcano's flanks (Chadwick & Howard, 1991). The stress field allowing the formation of both types of fissures seems to be mainly controlled by the gravitational unloading after caldera collapse and the stresses from previous intrusions (Bagnardi et al., 2013; Corbi et al., 2015, 2016), with further contribution from the load of the edifice and the pressurization of a flat-topped magma chamber (Chadwick & Dieterich, 1995).

Before the last eruption in 2008, 10 witnessed eruptions have occurred at Cerro Azul since 1932. During the previous two eruptions (1979 and 1998), radial eruptive fissures opened in the same area (eastern flank) as the 2008 eruption (Mouginis-Mark et al., 2000; Naumann & Geist, 2000; Rowland et al., 2003; Teasdale et al., 2005).

The 2008 eruption of Cerro Azul occurred in two phases (Global Volcanism Program, 2008). The first phase (from 29 May to 1 June) began with the effusion of a lava flow from an eruptive fissure immediately outside the eastern caldera rim (Figure 1c). Subsequently, further eruptive fissures opened on 30 May, parallel to the former, on the eastern upper flank (Figure 1c). All these fissures ceased their effusive activity by 1 June. The second eruptive phase (3 June to 11 June) was characterized by effusive activity from a new radial fissure located in a flatter area near the edge of the lower eastern flank of Cerro Azul (Figure 1).

3. Methods

3.1. InSAR Data Processing

To measure surface deformation before, during, and after the 2008 eruption at Cerro Azul, we used InSAR data. We generated 79 SAR images acquired by the European Space Agency's ENVISAT satellite (C-band, wavelength $\lambda = 5.63$ cm), 32 from an ascending track (T61) acquired between January 2006 and May 2010, and 47 from a descending track (T140) acquired between January 2003 and May 2010. We also generated 33 SAR images from the Japanese Space Agency's ALOS-1 satellite (L-band, wavelength $\lambda = 23.6$ cm), 17 from an ascending track (T133) acquired between March 2007 and March 2011, and 16 from a descending track (T474) acquired between March 2007 and July 2010.

We first generated interferograms with the InSAR Scientific Computing Environment software (Rosen et al., 2012). We removed topographic contributions to the interferometric phase using a 30 m-resolution DEM from the NASA Shuttle Radar Topography Mission (Farr et al., 2007). Then, to study the temporal evolution of surface displacements, we combined interferograms through a multi-temporal approach. In particular, we

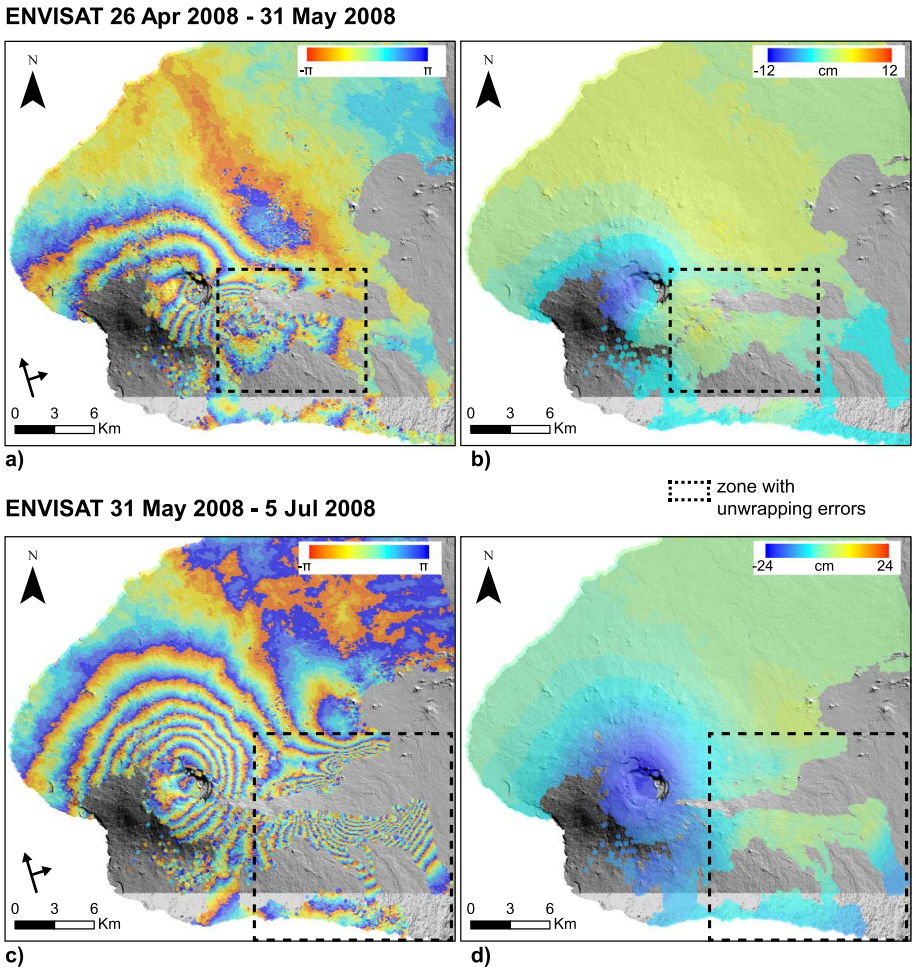

Figure 2. Comparison between (a,c) wrapped and (b,d) unwrapped images from ENVISAT ascending track 61. Dashed rectangles highlight areas with an incorrect unwrapping, where the opening displacement across the eruptive fissure is not visible. In (a) and (c), each fringe (full color cycle) represents 2π radians of phase change corresponding to 2.8 cm of range change in the line-of-sight (LOS) direction.

adopted the small baseline (SB) method using the StaMPS software (Hooper, 2008; Hooper et al., 2012) and selected the processing parameters that maximized the signal-to-noise ratio. In the supporting information Table S1, we report a list of the network of interferograms used for the SB analysis.

3.2. Geodetic Modelling

To interpret InSAR phase in terms of a geophysical model, it is necessary to estimate the integer ambiguities in the phase (phase unwrapping). This is generally done prior to geophysical inversion, but any phase-unwrapping error will bias the resulting geophysical parameters. This would be the case for the ENVISAT data (Figure 2), where the three-dimensional unwrapping routine of StaMPS (Hooper, 2010a) cannot adequately unwrap data in the distal region where the radial eruptive fissures opened. This is evident when comparing displacements in the ENVISAT data near the eruptive fissures to those in the ALOS-1 interferogram in Figure 3d. To overcome this problem, we adopted a method to model the wrapped phase data directly, by estimating the integer ambiguities simultaneously with the geophysical parameters (Hooper, 2010b). We applied a Markov chain Monte Carlo method to build the posterior probability of the model, conditional on the data.

According to the Bayes' theorem, the probability density function (PDF) of the vector of model parameters, $\mathbf{m}$, given data vector, $\mathbf{d}$, $p(\mathbf{m}|\mathbf{d})$, is (1)

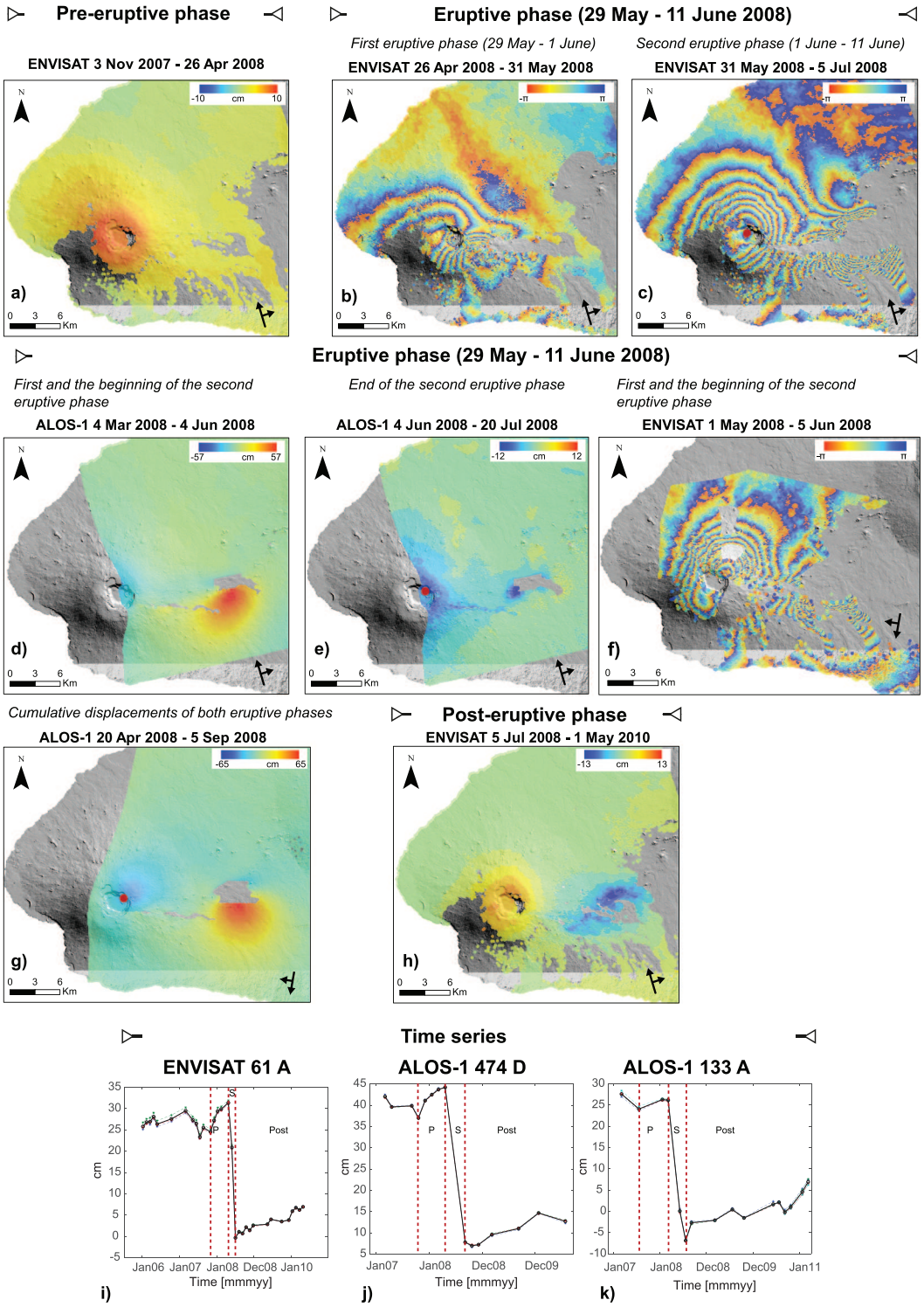

Figure 3. Time-series results. (a–c) ENVISAT LOS displacement map for ascending orbit 61 during (a) pre-eruption (November 2007–April 2008); (b) first eruptive phase; (c) second eruptive phase . (d–e) ALOS-1 LOS displacement map for ascending orbit 133, during the eruption. (f) ENVISAT LOS displacement map for descending track 140. (g) ALOS-1 LOS displacement map for descending track 474 (April–September 2008). (h) ENVISAT LOS displacement map for ascending track 61 during the post-eruptive period (July 2008–May 2010). (i–k) Time series, with the dotted red lines that separate the pre-eruptive period (*P*), the sin-eruptive period (*S*), and the posteruptive period (Post). The red dot in Panels c, e, and g indicate the location for which deformation time series are shown respectively in Panels i, k, and j. In (a), (d–e), and (g–h), data are unwrapped, and spatially correlated look-angle errors (including orbital ramps) are removed. In (b–c) and (f), data are wrapped, and each fringe (full color cycle) represents 2π radians of phase change corresponding to 2.8 cm of range change in the line-of-sight direction. All the displacement maps are overlaid onto shaded relief map from WorldDEM data.

$$p(\mathbf{m}|\mathbf{d}) = \frac{p(\mathbf{d}|\mathbf{m})p(\mathbf{m})}{\int_{-\infty}^{\infty} p(\mathbf{d}|\mathbf{m})p(\mathbf{m})\mathrm{d}\mathbf{m}} \quad (1)$$

Where $p(\mathbf{d}|\mathbf{m})$ is the likelihood function, $p(\mathbf{m})$ is the prior distribution for the model parameters, and the denominator is a normalizing constant. For a given discrete inverse problem, data and model vectors are related by a function g plus error $\mathbf{e}$ (2):

$$\mathbf{d} = g(\mathbf{m}) + \mathbf{e} \quad (2)$$

Thus, to calculate the likelihood function, the PDF of $\mathbf{e}$ is required. In the InSAR data, after the SB analysis with StaMPS, the errors are correlated, principally due to the contribution from variable atmospheric propagation delay (e.g., Hanssen et al., 1999). While the univariate PDF for a single wrapped phase value can be reasonably expected to follow a wrapped normal distribution, the multivariate PDF for correlated wrapped data is difficult to calculate. We simplify the problem by calculating the wrapped phase differences for arcs between nearby coherent pixels. For coherent pixels, the contribution of uncorrelated noise to the arc phase is small (compared to a phase cycle) and reasonably approximated by a Gaussian distribution (Just & Bamler, 1994). As long as the pixels are nearby, the atmospheric contribution (and any other spatially correlated error) to the arc phase is also small and reasonably approximated by a Gaussian distribution. Thus, we approximate the joint PDF with a multivariate Gaussian distribution, with the likelihood function given by (3):

$$\mathrm{p}(\mathbf{d}|\mathbf{m}) = (2\pi)^{-N/2}|\boldsymbol{Q}_d|^{-1/2}e^{-\frac{1}{2}\left\{ W\{\mathbf{d}-g\{\mathbf{m}\}\}^T\mathbf{Q}_d^{-1}W\{\mathbf{d}-g\{\mathbf{m}\}\}\right\}} \quad (3)$$

where $W\{.\}$ is the wrapping operator, $\mathbf{d}$ now represents wrapped arc phase values, N is the dimension of $\mathbf{d}$, and $\mathbf{Q}_\mathrm{d}$ is the variance-covariance matrix for the errors in the arc phase values.

As InSAR data sets contain a large number of measurement points, to reduce computational time, we subsample the data set prior to generating the network of arcs. For the best results, it is essential to use an algorithm that maintains a good data point density in the deformed area. To this end, we use the adaptive quadtree sampling algorithm of Geodetic Bayesian Inversion Software (GBIS) (see Bagnardi & Hooper, 2018 and Decriem et al., 2010 for details) modified so that in each iteration the mean wrapped phase for the all pixels in the polygon is found. If the wrapped difference between the mean and phase of any pixel is greater than a threshold value (default $\pi/2$), the polygon is subdivided into smaller polygons. This differs from the standard algorithm, which thresholds on standard deviation of phase values.

We generate the network of arcs using the Euclidean minimum spanning tree method (Kruskal, 1956; Prim, 1957). This method minimizes the total length of the arcs and avoids introducing unnecessary redundancy in the measurements; in other words, the model values for all arc phase values remain independent. The Euclidean minimum spanning tree leads to a network with every pixel connected to at least one other and without isolated subsets (Figure 4c). We assume that the only correlation between arc phase errors is due to the contribution of spatially uncorrelated noise to arcs connected by the same pixel. This means that we ignore any potential correlation due to the atmospheric contribution to the errors. This may not be negligible in areas of steep topography, where the hydrostatic tropospheric contribution to the arc phase errors could be significant and correlated between arcs, but it is likely reasonable for our application to the gently sloping flanks of Cerro Azul.

We quantify the error structure of the data in the conventional way using the fitVariogram function of GBIS (Bagnardi & Hooper, 2018) applied to an undeformed region of the interferogram, where phase unwrapping is typically not problematic. Once estimated using the fitVariogram function, we use the nugget, sill, and range values to set up the variance-covariance matrix; we set the elements of the main diagonal (σ_{ii}^2) as (4):

$$\sigma_{ii}^2 = 2\text{*nugget} + 2\text{*sill*}[1-\exp(-3\text{*h/range})] \quad (4)$$

where h is the length of the arc that connects each pair of pixels. We set the off-diagonal terms to the nugget value for arcs that share a pixel and zero otherwise. Then we convert the variance and covariance values

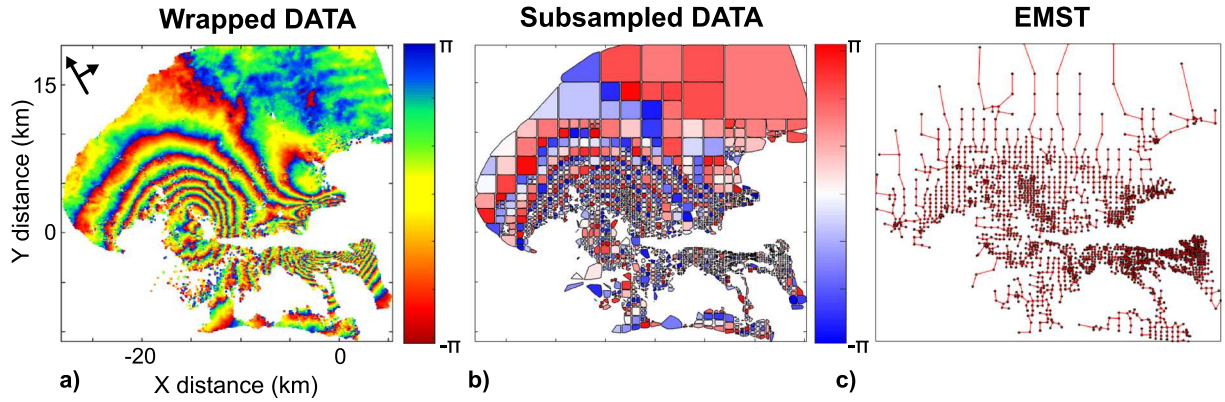

Figure 4. (a) Wrapped InSAR data from ENVISAT ascending track 61, acquired from 31 May to 5 July 2008. Each fringe (full color cycle) represents 2π radians of phase change corresponding to 2.8 cm of range change in the line-of-sight direction. (b) Downsampled data using our modified quadtree function. (c) The arcs formed by the Euclidean minimum spanning tree (EMST).

from m^2 to rad^2. We do not consider potential model errors in this study, but they could be incorporated into the variance-covariance matrix using the approach of Duputel et al. (2014).

Once we have defined the arcs and variance-covariance matrix for our quadtree-sampled data set, we estimate the posterior PDF of model parameters and uncertainties using the Bayesian approach implemented in the GBIS software (Bagnardi & Hooper, 2018), which uses a Markov chain Monte Carlo method, incorporating the Metropolis Hastings algorithm and which we modified for working with the phase difference instead of unwrapped LOS displacements.

Therefore, with this method, the integer ambiguities in the phase are not explicitly solved for, but a probability distribution of integer ambiguities for each pixel is a by-product of the inversion.

We tested this method on synthetic data and validated it by comparing the results to those from GBIS. We modeled the sources using the rectangular dislocation (RD) model of Nikkhoo et al. (2017) and set the "plunge angle" $\theta = 0$ (see Nikkhoo et al., 2017 for further details) so that the two uppermost corners of the dike/inclined sill are at the same depth. In this configuration, the RD model becomes almost equal to the Okada (1985) solution (Nikkhoo et al., 2017). For all modelling, we assumed an isotropic elastic half-space with Poisson's ratio of 0.25. To achieve convergence of the posterior PDF, we found it necessary to perform half a million iterations.

4. Data Description

4.1. Pre-Eruption

InSAR time series of ENVISAT ascending and ALOS-1 descending data record a pre-eruptive uplift of ~10–12 cm, peaking immediately outside the western portion of the caldera, and occurring from October 2007 to April 2008, before the eruption started on 29 May (Figures 3a and 3i–3j). The inflation slows in the months just before the eruption (Figures 3i–3j). The temporal resolution of the InSAR data does not shed light on whether this uplift continued until just prior to the eruption or not.

4.2. Eruption

ENVISAT ascending data allow us to separate the deformation of the two eruptive phases. Until 31 May (the end of the pre-eruptive phase plus the first eruptive phase), these data record a subsidence of ~12 cm in the western sector of the caldera and in the west and south-western sectors of the upper flank of the volcano, peaking in the same area of the maximum uplift of the pre-eruptive period (Figure 3b). LOS displacements of about the same magnitude, but opposite in sign, occurred near the active eruptive fissures, placed on the upper east flank (Figure 3b). After 31 May (the second eruptive phase plus the beginning of the posteruptive phase; Figures 3c–3g), there is an eastward shift of the subsidence on the volcano summit, with another 24 cm of subsidence peaking in the caldera area (Figures 3c–3e). At the same time, the deformation on the east flank migrated from the summit vents, which ceased their activity on 1 June, to the distal radial fissure at the

base of the eastern flank, which started its activity on 3 June. Most of this deformation (~60 cm) occurred by 4 June (Figures 3d–3f), even if the eruptive fissure remained active until 11 June. Conversely to ENVISAT data, ALOS-1 descending data (Figure 3g) maintain good coherence on the southern flank of Cerro Azul, even though they are less well sampled temporally, and show a lower amount of subsidence (~15 cm) with respect to the proximal area (~38 cm).

4.3. Posteruption

After the eruption, from July 2008 to March 2011 there was a new uplift of the caldera area, characterized by nonuniform rates (Figures 3h–3k). The temporal resolution of our InSAR data does not allow us to better constrain the onset of uplift.

5. Tests on the Synthetic and Real Data

To test the validity of the method described in section 3.2, we performed a test on synthetic data. We used a data coverage similar to that of ENVISAT data in the area of the dike (Figures 2c and S1). We calculated the phase due to displacements caused by an RD dike source (model parameters reported in Figure 6 and Table S2), assuming wavelength of 0.0563 m, an incidence angle of 25.71° and a heading angle of 12.3992° (Figure S1a). We added a realistic atmospheric phase screen error using an isotropic two-dimensional fractal surface with power-law behavior (Hanssen, 2001; Figure S1b) and random noise (Figure S1c) to simulate noncorrelated errors. Then we inverted the synthetic data using both the method described in section 3.2 (Figures 5a–5c) and GBIS (Figures S2a–S2c) and compared the results (Figure 6; Table S2). Results show that the actual model parameters fall within the 95% bounds of the posterior PDFs (Figure 6), with the latter consistent with GBIS results, confirming the applicability of the method. In Figures S3 and S4, we show the trace plot, obtained with the new method and with GBIS, in which it is possible to evaluate the convergence of the Markov chain. In both cases, the number of early samples that strongly depend on the choice of the starting value (the so-called "burn-in" period) is similar. This is due also to the fact that the new method uses the same MCMC algorithm as GBIS, with the main difference being that the wrapped phase differences between pixels are used to constraint the model rather than the LOS displacements.

We also performed tests on real data. First, we applied this new method to a real case that can be easily unwrapped, by performing a joint inversion of the deformation recorded in ALOS-1 ascending and descending data on the east flank of Cerro Azul (Figures 3d and 3g). We compared these results to those obtained with GBIS, finding an overall consistency (Figures 5d–5i, S2d–S2i, and S5 and Table S3), again supporting the method proposed in section 3.2. Finally, we applied the new method to invert the unwrapped phase of data that are affected by unwrapping errors (the ENVISAT ascending data; Figures 2c and 5j). Results (Figures 5j–5l, Figure S6, and Table S4) are consistent with those obtained from the inversion of ALOS-1 data, further confirming the applicability of the method to measurements that cannot easily be unwrapped without errors and so cannot be inverted with GBIS (Figure S7 and Table S5).

6. Results of the Geodetic Modelling

6.1. Pre-Eruptive Phase

We modeled the pre-eruptive uplift occurred at Cerro Azul recorded by ALOS-1 descending track data (19 October 2007–20 April 2008) for possible magmatic sources using the standard GBIS software applied to unwrapped interferogram. Best results were obtained using a Mogi source (Figures 7a–7c and S8, Table 1). The Bayesian analysis converged to an inflation point, placed at ~5 km below the north caldera rim, with a volume change (ΔV) = $12.6 \pm 3.7 \times 10^{-3}$ km^3 and a corresponding injection rate of $2.5 \pm 0.7 \times 10^{-2}$ km^3/year.

6.2. Eruptive Phase

ENVISAT ascending data are the only that allow us to distinguish the deformation of the first eruptive phase from that of the second phase. Thus, we use these data to constrain the sources of deformation of the two phases. As we were not able to reliably unwrap these interferograms, we used the wrapped inversion method described in section 3.

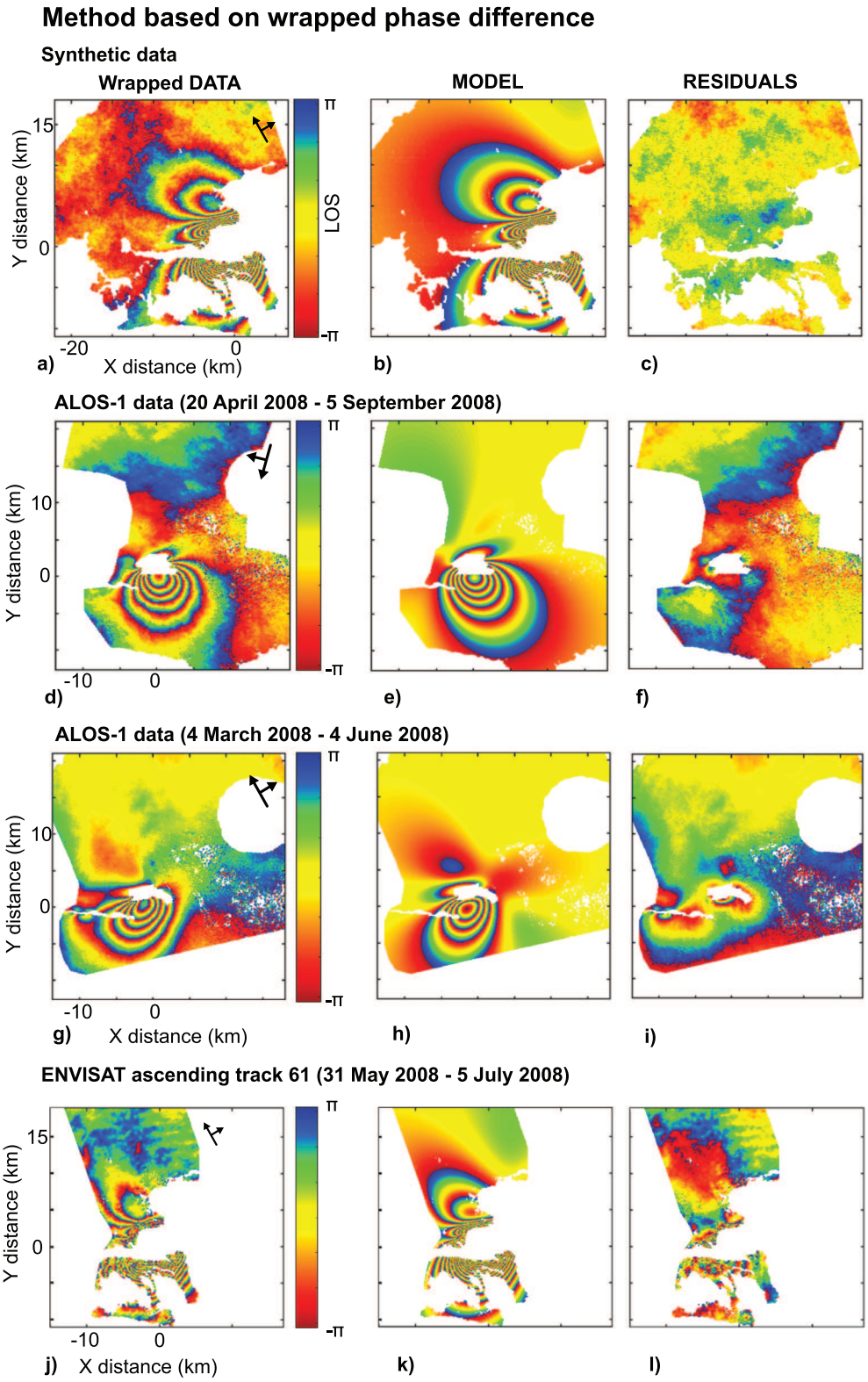

Figure 5. (a) Simulated wrapped data. (b) Predicted displacements for the RD model using the MAP solution (Table S2). (c) Related residuals. (d,g) Wrapped ALOS-1 data for descending track 474 (d,j) wrapped ALOS-1 data for the ascending track 133. (j) Wrapped ENVISAT data from ascending track 61. (e,h,k) Predicted displacements for the RD model using the MAP solution (see Tables S3 and S4). (f,i,l) Related residuals. Each fringe (full color cycle) represents 2π radians of phase change corresponding to 2.8 cm of range change in the LOS direction in Panels a–c and j–l and to 11.8 cm of range change in the LOS direction in Panels d–i. The local origin for Panels d–l is 91°26′W and 0°93′S.

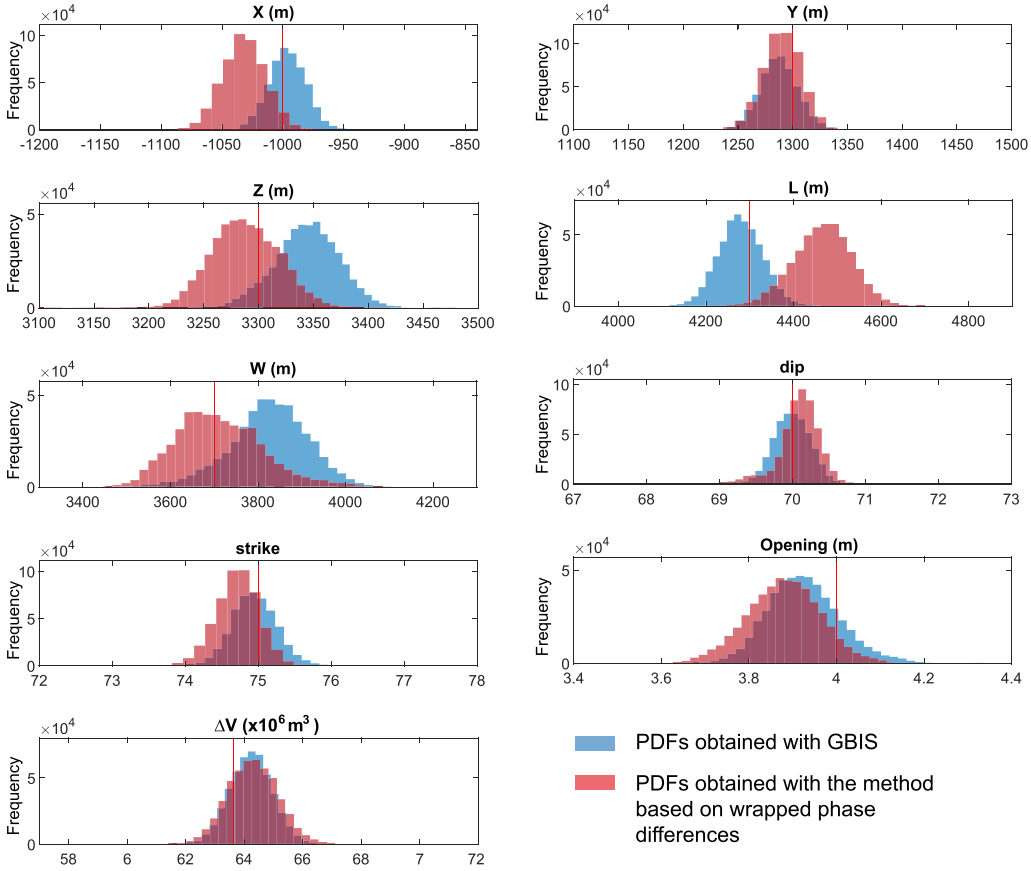

Figure 6. Posterior probability density distribution (PDFs) for each individual model parameter from the inversion of the synthetic data using both our new method and GBIS. The red lines representing the actual simulated values (see Table S2).

6.2.1. April–31 May (End of the Pre-Eruptive Phase Plus the First Eruptive Phase)

We modeled deformation during the first phase using a combination of two RD sources (Figures 8a–8c, S9; Table 2). The first dislocation converged to a 9×1 km horizontal sill, with the major axis oriented northeast-southwest, placed at ~5.2 km below the western sector of the caldera and the flank of the volcano. The modeled sill shows a contraction of 1.1 ± 0.2 m, with a corresponding volume change of $\Delta V = -11.2 \pm 0.6 \times 10^{-3}$ km^3. As for the second dislocation, the Bayesian analysis converged to an east-southeast oriented subvertical dike, whose top edge is placed at ~2.8 km below the eastern flank, with an opening of 1.1 ± 0.3 m. The corresponding ΔV is $9.9 \pm 0.5 \times 10^{-3}$ km^3. This dike explains most of the deformation recorded on the east flank by the InSAR data in this period, but it is placed ~2 km to the north of the active eruptive fissures of the first phase, and its geometry (southward dipping) and position do not seem compatible with the location and orientation of the eruptive fissures. There is no obvious geodetic signal associated with these eruptive fissures, and we infer that it is probably hidden by that of the radial dike, which dominates the deformation field. The small residuals near the summit eruptive vents, which cannot be explained by our model, may be the remains of the geodetic signal related to these eruptions.

6.2.2. 31 May–5 July (Second Eruptive Phase and Beginning of the Posteruptive Phase)

To model the second eruptive phase, we again used two RD sources (Figures 8d–8f and S10; Table 2). The Bayesian analysis results in a larger 9×7 km deflating sill, placed below the caldera. The corresponding volume loss is $25 \pm 2.2 \times 10^{-3}$ km^3. To reduce the number of variables and to better constrain the opening and the length and width of this sill, we fixed the sill depth using the depth of the sill obtained from the inversion of the data of the first eruptive phase. The opening of a N80° south-southeast-dipping dike (dip angle = 68°), whose top is at ~0.9 km below the radial distal eruptive fissure, explains the distal deformation. The volume change of this dike is $57.4 \pm 2.6 \times 10^{-3}$ km^3. Most of this volume was probably emplaced by 4

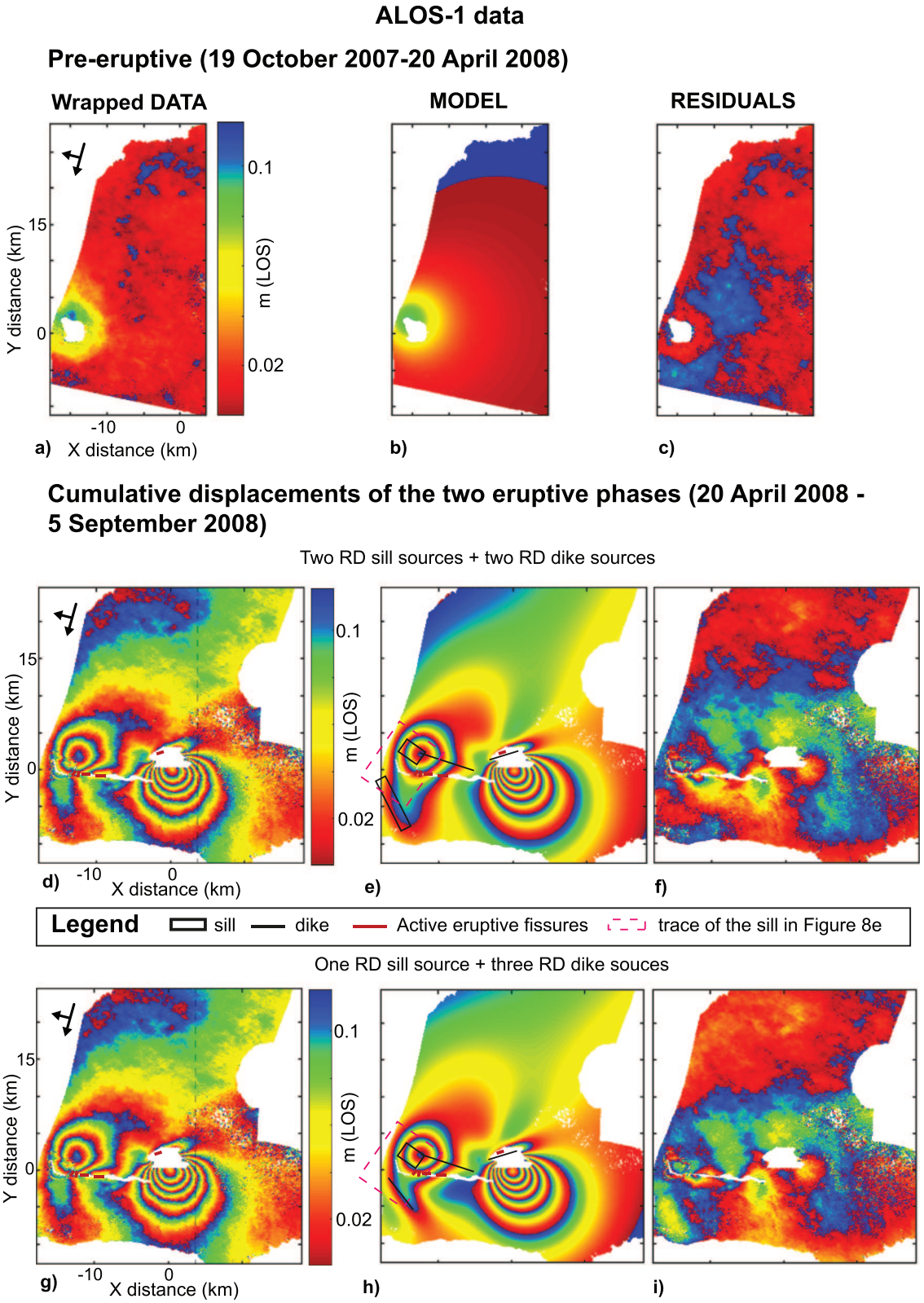

Figure 7. (a,d,g) Wrapped ALOS-1 LOS displacements for descending track 474. Each fringe (full color cycle) represents 11.8 cm of LOS displacement. (b) Predicted displacements for the Mogi model. (c) Related residuals. (e,h) Predicted displacements for the four dislocation models using the maximum a posteriori probability solutions (MAP). (f,i) Related residuals. The surface projections of the dislocations are shown on Panel e. Dikes appear as lines as we drew only the projection of the top of the dislocation. The dotted gray line in Panel d delimits the area of the Panels a to c. The local origin for all panels is 91°26'W and 0°93'S.

Table 1
Results of the Bayesian Analysis for the ALOS-1 Descending Track Data

ALOS-1 data (descending track 474)										
Pre-eruptive (19 October 2007–20 April 2008)										
Mogi source										
	x (m)	y (m)	Depth (m)	ΔV ($\times 10^6$ m^3)						
Optimal	−16,962	2,202	4,905	11.66						
2.50%	−17,472	1,828	4,364	8.94						
97.50%	−16,602	2,560	5,815	16.29						
Prior lower	−20,000	−5,000	4,000	0.01						
Prior upper	−10,000	5,000	8,000	1,000						
Eruption (20 April–5 September 2008): 2 RD sill sources + 2 RD dike sources										
RD dike (first event)										
	x (m)[a]	y (m)[a]	z (m)[a]	L (m)[a]	W (m)[a]	θ[a]	Dip[a]	Strike[a]	Op.[a] (m)	ΔV ($\times 10^6$ m^3)
Optimal	−8,747	880	3,252	7,570	1,018	0	84	108	1.28	
2.50%	−8,747	880	3,252	7,570	1,018	0	84	108	1.28	
97.50%	−8,747	880	3,252	7,570	1,018	0	84	108	1.28	
Prior lower	−8,747	880	3,252	7,570	1,018	0	84	108	1.28	
Prior upper	−8,747	880	3,252	7,570	1,018	0	84	108	1.28	
RD dike (second event)										
	x (m)	y (m)	z (m)	L (m)	W (m)	θ[a]	Dip	Strike	Op. (m)	ΔV ($\times 10^6$ m^3)
Optimal	−990	1,205	3,538	4,051	4,829	0	75	73	3.53	69.1
2.50%	−1,051	1,103	3,268	3,960	4,091	0	73	72	3.33	61.2
97.50%	−945	1291	3,674	4,226	5,103	0	76	74	3.79	73.2
Prior lower	−10,000	−10,000	2,700	1,000	1,000	0	40	1	0	
Prior upper	10,000	10,000	4,000	6,000	5,200	0	85	90	5	
Northern RD deflated sill										
	x (m)	y (m)	z (m)[a]	L (m)	W (m)	θ[a]	Dip[a]	Strike[a]	Op. (m)	ΔV ($\times 10^6$ m^3)
Optimal	−13,523	2,304	5,200	2,025	3,007	0	0	35	−4.47	−27.2
2.50%	−13,679	2,169	5,200	2,006	3,004	0	0	35	−4.49	−29
97.50%	−13,383	2,454	5,200	2,757	3,511	0	0	35	−3.15	−25.5
Prior lower	−20,000	−10	5,200	2,000	3,000	0	0	35	−5.5	
Prior upper	−10,000	4,000	5,200	10,000	8,000	0	0	35	0	
Southern RD deflated sill										
	x (m)	y (m)	z (m)[a]	L (m)	W (m)	θ[a]	Dip[a]	Strike	Op. (m)	ΔV ($\times 10^6$m^3)
Optimal	−16,041	−4,611	5,200	1,433	7,473	0	0	63	−0.97	−10.38
2.50%	−16,487	−5,737	5,200	514	6,295	0	0	47	−2.96	−13.3
97.50%	−15,297	−3,875	5,200	2,390	7,786	0	0	77	−0.6	−7.8
Prior lower	−18,000	−8,000	5,200	500	6,000	0	0	10	−3.5	
Prior upper	−13,500	−1,000	5,200	3,000	7,800	0	0	89	0	

Note. x and y are the local coordinates of the Mogi source and of the center of the RD source with respect to a local origin (see Figure 7) at 91°26′ W and 0°93′S. Depth (z) is referred to the center of the RD and is with respect to the surface (positive downward). ΔV is the volume change (for the RD source it is calculated with the formula $\Delta V = L * W *$ Op). θ is the angle between the RD upper edge and the intersection of the RD plane with the free surface. L and W are the length and width of the RD source. Op. is the opening (see Nikkhoo et al., 2017, for a better explanation of the RD parameters). Optimal is the maximum a posteriori probability solution. 2.50% and 97.50% are the percentile values describing the credible interval. Prior lower and upper are the bounds of the prior distribution used for the inversion.
[a]Fixed parameter.

June, as ALOS-1 ascending data (Figures 3d–3e) indicate that most of the related deformation occurred by 4 June. This radial dike lies on the continuation of the radial dike of the first phase, even though with an anticlockwise rotation of about 28° and a decrease in the dip angle (68° compared to 84°).

6.2.3. ALOS-1 Data: 20 April–5 September (Cumulative Displacements of the Two Eruptive Phases)

ALOS-1 descending track data are less temporally constrained than the ENVISAT data, recording the cumulative deformation pattern of the 2008 eruption but maintain good coherence on the southern flank. Therefore, we inverted the ALOS-1 data using the GBIS software. To allow for multiple different sources as indicated by the ENVISAT results, we inverted for four RDs (Figures 5d–5f, S11; Table 1).

We modeled the deformation at the base of the east flank of Cerro Azul with a dike. We set uninformative prior PDFs for each model parameter of this dike (Table 1). As deformation from the radial dike in the first eruptive phase is masked by the subsequent deformation, we fixed the parameters for it to the MAP solution from the ENVISAT results. We allowed for only one sill to fit the deformation beneath the caldera during

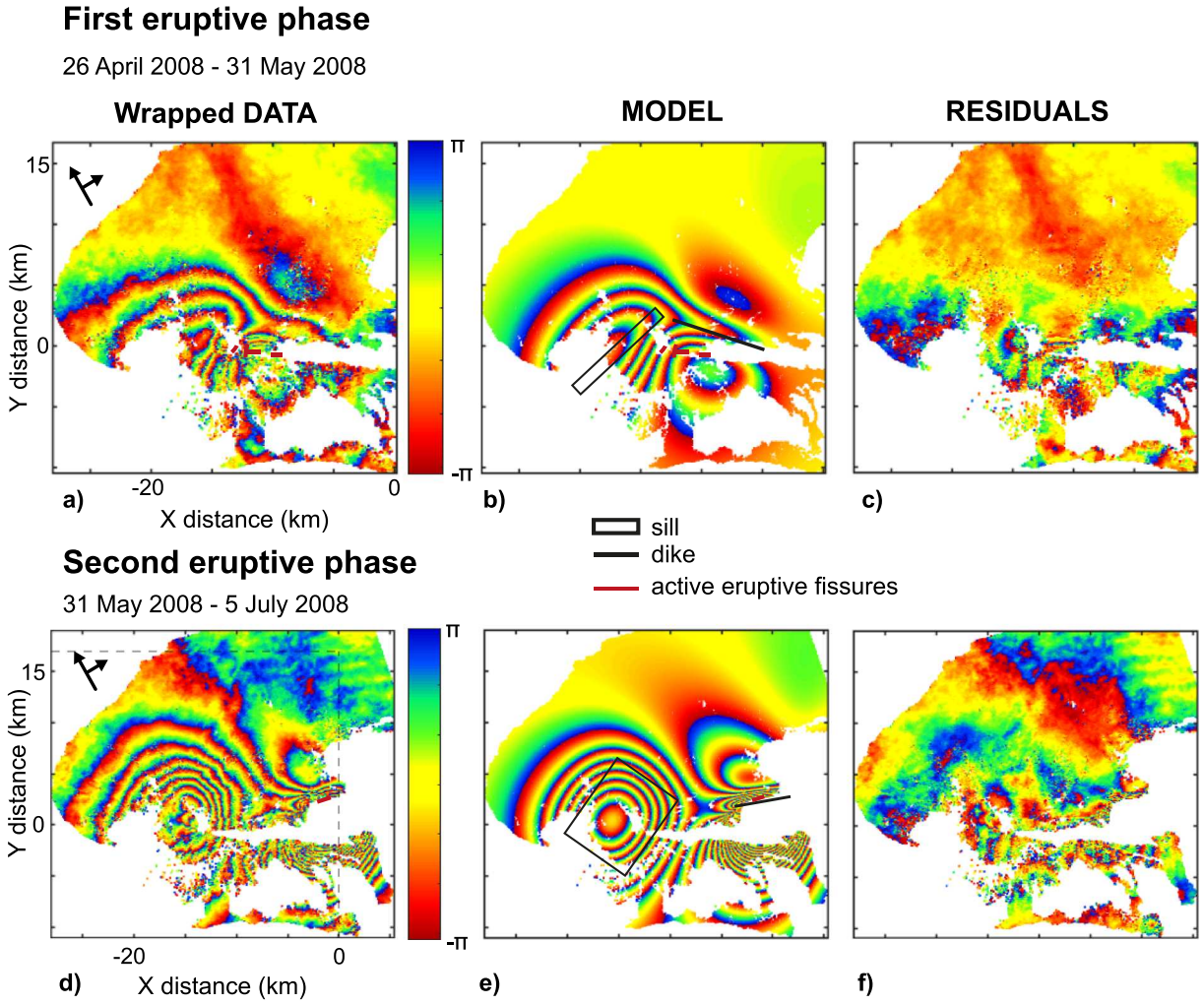

Figure 8. (a) Wrapped ENVISAT phase for ascending track 61 for the first eruptive period and (d) for the second eruptive period. Each fringe (full color cycle) represents 2π radians of phase change corresponding to 2.8 cm of range change in the LOS direction. (b,e) Predicted displacements for the respective two RD models using the MAP solutions. (c,f) Related residuals. The surface projections of the dislocations are shown on Panels b and e. Dikes appear as lines as we drew only the projection of the top of the dislocation. The local origin for all panels is 91°26′W, 0°93′S. The dotted gray line in Panel d delimits the area of the Panels a to c.

both eruptive phases in the ENVISAT data, as the locations are the same within error. We also added a second sill beneath the south flank of Cerro Azul, an area not covered by the ENVISAT data, as there is deformation visible there in the ALOS data.

The results for the unconstrained dike converged to a south-southeast-dipping dike (dip angle ~75°), with a $\Delta V = 67.2 \pm 6 \times 10^{-3}$ km^3, which is about 22% more than estimated from the ENVISAT data inversion. This discrepancy is due to the inversion of only one ALOS-1 descending track; this records a higher magnitude of the LOS displacements in that area than the ascending tracks of ALOS-1 and ENVISAT. Results from the joint inversion of the ALOS-1 ascending and descending track (Figures 5d–5i and S2d–S2i; Table S3) are in fact consistent with the volume estimated from the inversion of ENVISAT data.

The two sills largely overlap the sill resulting from the modelling of the second eruptive phase from the inversion of ENVISAT data (Figure 7e). However, the sill on the southern flank shows less contraction (-1.8 ± 1.2 m) with respect to the sill below the caldera (-3.8 ± 0.7 m). The total volume lost by the two sills is approximately equal to the sum of the volume loss from the inversion of ENVISAT data during the two eruptive phases (Tables 1 and 2) ($-37.8 \pm 4.5 \times 10^{-3}$ km^3 with respect to $-36.2 \pm 2.8 \times 10^{-3}$ km^3 of ENVISAT data).

Table 2
Results of the Bayesian Analysis for the Inversion of ENVISAT Ascending Track Data

ENVISAT ascending track 61. April–May 2008 (first eruptive phase)										
RD radial dike										
	x (m)	*y* (m)	*z* (m)	*L* (m)	*W* (m)	θ[a]	Dip	Strike	Op. (m)	ΔV ($\times 10^6$ m^3)
Optimal	−8,747	881	3,252	7,569	1,019	0	84	108	1.29	9.9
2.50%	−8,942	776	3,182	7,005	1,001	0	83	108	0.79	9.4
97.50%	−8,603	925	3,325	7,895	1,683	0	85	110	1.41	10.4
Prior lower	−12,500	100	2,100	1,000	1,000	0	40	80	0	
Prior upper	−5,000	5,000	5,000	10,000	4,000	0	89	270	5	
RD deflating sill										
	x (m)	*y* (m)	*z* (m)	*L* (m)	*W* (m)	θ[a]	Dip	Strike	Op. (m)	ΔV ($\times 10^6$ m^3)
Optimal	−16,964	−458	5,188	9,365	1,001	0	0	43	−1.23	−11.5
2.50%	−17,053	−517	5,026	8,695	1,003	0	0	41	−1.24	−11.8
97.50%	−16,864	−130	5,319	9,727	1,415	0	2	49	−0.88	−10.6
Prior lower	−21,000	−5,000	3,200	2,000	1,000	0	0	1	−5	
Prior upper	−10,000	5,000	6,000	12,000	12,000	0	30	360	0	
ENVISAT ascending track 61. May–July 2008 (second eruptive phase)										
RD radial dike										
	x (m)	*y* (m)	*z* (m)	*L* (m)	*W* (m)	θ[a]	Dip	Strike	Op. (m)	ΔV ($\times 10^6$ m^3)
Optimal	−593	1,234	2,985	5,564	4,529	0	68.4	80	2.25	56.7
2.50%	−632	1,161	2,915	5,441	4,349	0	67.6	79	2.17	54.8
97.50%	−512	1,268	3,139	5,749	4,878	0	68.9	81	2.31	61
Prior lower	−6,000	−2,000	2,800	1,000	1,000	0	50	1	0	
Prior upper	5,000	4,000	5,000	5,800	5,200	0	86	89	5	
RD deflating sill										
	x (m)	*y* (m)	*z* (m)[a]	*L* (m)	*W* (m)	θ[a]	Dip	Strike	Op. (m)	ΔV ($\times 10^6$ m^3)
Optimal	−14,889	603	5,200	9,009	7,231	0	0	35	−0.39	−25.4
2.50%	−15,069	395	5,200	8,271	6,428	0	−3	24	−0.43	−27.2
97.50%	−14,714	953	5,200	9,470	7,813	0	5	48	−0.37	−22.8
Prior lower	−21,000	−5,000	5,200	1,000	1,000	0	−30	1	−5	
Prior upper	−10,000	5,000	5,200	14,000	14,000	0	30	90	0	

Note. For the meaning of the parameters, see note in Table 1.
[a]Fixed parameter.

6.2.4. Joint Inversion of ALOS-1 and ENVISAT Data

We jointly inverted the descending data of ALOS-1 and the total deformation recorded by ENVISAT ascending track, to better constrain the deformation source parameters, allowing for two dikes and two sills (Figure S12; Table S6). In this inversion, we combined the use of unwrapped data for ALOS-1 and wrapped data for ENVISAT. For the radial dike of the first eruptive phase, we again fixed the geometry using the MAP solution from the inversion of ENVISAT data for the first eruptive phase but now inverting for the opening.

Results of the Bayesian analysis (Table S6) converge to solutions similar to the other models. In the area near the caldera, residuals are larger than those from the single track inversions (Figure S12) due to the requirement to also fit the ALOS-1 data.

6.2.5. ALOS-1 Data: 20 April–5 September (Cumulative Displacements of the Two Eruptive Phases)

Finally, we inverted the ALOS-1 descending data with GBIS using also a different combination of sources (one RD sill and three RD dikes), to test if the subsidence on the southern flank could be modeled with a dike. As for the dikes on the eastern flank, we made the same assumptions done in the inversion reported in section 6.2.3 (Table 1).

Results of the Bayesian analysis (Figures 7g–7i and S13; Table 3) converge to a southeast oriented vertical dike, placed at 4.2 ± 0.6 km below the southern flank of Cerro Azul (Figure 7h), with a $\Delta V = 29.9 \pm 8.7 \times 10^{-3}$ km^3, providing therefore an alternative source to that inferred in section 6.2.3. As the descending track data of ENVISAT (Figure 3f), acquired from 1 May to 5 July 2008, show a similar deformation pattern in that area, this dike probably propagated during the second eruptive phase. As for the other sources, the results of the Bayesian analysis (Table 3) converge to solutions similar to those in section 6.2.3. Interestingly, the sill

Table 3
Results of the Bayesian Analysis for the ALOS-1 Descending Track Data

ALOS-1 data (descending track 474)										
Eruption (20 April–5 September 2008): 1 RD sill source + 3 RD dike sources										
RD dike (first event)										
	x (m)[a]	y (m)[a]	z (m)[a]	L (m)[a]	W (m)[a]	θ[a]	Dip[a]	Strike[a]	Op.[a] (m)	ΔV ($\times 10^6$ m^3)
Optimal	−8,747	880	3,252	7,570	1,018	0	84	108	1.28	
2.50%	−8,747	880	3,252	7,570	1,018	0	84	108	1.28	
97.50%	−8,747	880	3,252	7,570	1,018	0	84	108	1.28	
Lower	−8,747	880	3,252	7,570	1,018	0	84	108	1.28	
Upper	−8,747	880	3,252	7,570	1,018	0	84	108	1.28	
RD dike (second event)										
	x (m)	y (m)	z (m)	L (m)	W (m)	θ[a]	Dip	Strike	Op. (m)	ΔV ($\times 10^6$ m^3)
Optimal	−995	1,201	3,501	4,080	4,703	0	74	73	3.55	68.1
2.50%	−1,045	1,075	3,234	3,962	3,695	0	72	72	3.29	59.8
97.50%	−931	1,266	3,712	4,225	5,177	0	75	74	3.83	73.7
Lower	−10,000	−10,000	2,700	1,000	1,000	0	40	1	0	
Upper	10,000	10,000	4,000	6,000	5,200	0	85	90	5	
RD deflated sill										
	x (m)	y (m)	z (m)[a]	L (m)	W (m)	θ[a]	Dip[a]	Strike[a]	Op. (m)	ΔV ($\times 10^6$ m^3)
Optimal	−13,423	1,875	5,200	2,120	3,003	0	0	35	−4.89	−31.1
2.50%	−13,591	1,804	5,200	2,009	3,004	0	0	35	−5.1	−33.2
97.50%	−13,282	2,123	5,200	3,167	3,491	0	0	35	−2.81	−28.4
Lower	−20,000	−10	5,200	2,000	3,000	0	0	35	−5.5	
Upper	−10,000	4,000	5,200	10,000	8,000	0	0	35	0	
SouthernRD dike										
	x (m)	y (m)	z (m)[a]	L (m)	W (m)	θ[a]	Dip	Strike	Op. (m)	ΔV ($\times 10^6$ m^3)
Optimal	−15,015	−3,357	3,840	5,514	1,846	0	89.7	142	2.35	23.9
2.50%	−15,740	−3,938	3,562	5,506	1,020	0	87.5	137	1.47	18.2
97.50%	−14,596	−2,914	4,750	6,369	2,883	0	89.9	152	5.12	35.6
Lower	−18,000	−8,000	3,000	5,500	1,000	0	40	91	0.1	
Upper	−13,500	−1,000	5,000	9,000	3,200	0	90	179	9	

Note. For the meaning of the parameters, see note in Table 1.
[a]Fixed parameter.

placed below the caldera shows a volume loss of $\Delta V = -30.8 \pm 2.4 \times 10^{-3}$ km^3 that it is almost equal to the total volume loss by the system in the solution with two deflating sills (section 6.2.3 and Tables 1 and 3).

7. Discussion

The use of InSAR data and their geodetic modelling allows us to reconstruct the evolution of the 2008 eruption at Cerro Azul. Pre-Eruptive uplift of the caldera area during the 7 months before the eruption (Figures 9a–9b) seems related to the supply of new magma and is modeled with the inflation of a point source at ~5 km below the caldera. On 29 May, the first eruptive phase started. During this phase, the lateral propagation of a subvertical dike triggered the deformation on the eastern flank, while the observed subsidence is modeled with the deflation of a sill, placed below the western portion of the caldera and the upper western flank (Figures 9c–9d). The depth of this sill (~5 km below the surface) is consistent with the depth of both the modeled pre-eruptive point source and the magmatic reservoir of Cerro Azul, deeper than the other western Galápagos calderas (Geist et al., 2014). Therefore, the pre-eruptive uplift and the coeruptive subsidence are probably related to the inflation/deflation of the magmatic reservoir. The fact that we have modeled the reservoir with different simple sources reflects the complexities of the true magma reservoir, which may respond in various ways during the different inflation/deflation events (Edmonds et al., 2019; Sparks et al., 2019). Therefore, more complex geometries of the magma reservoir cannot be excluded (Yun et al., 2006). The modeled dike is placed ~2 km to the north of the eruptive fissures active during this phase, and its geometry and position do not seem compatible with the location of these fissures. Rather, the position of this dike (Figures 9e–9f), indicates it is the western, proximal portion of the radial dike responsible for the second eruptive phase, suggesting that the two segments form a single continuous intrusion. Thus, most of the deformation along the east flank of the first phase seems related to the incipient propagation of the radial dike of the second eruptive phase. During the first phase, the volume of the radial dike is similar to the

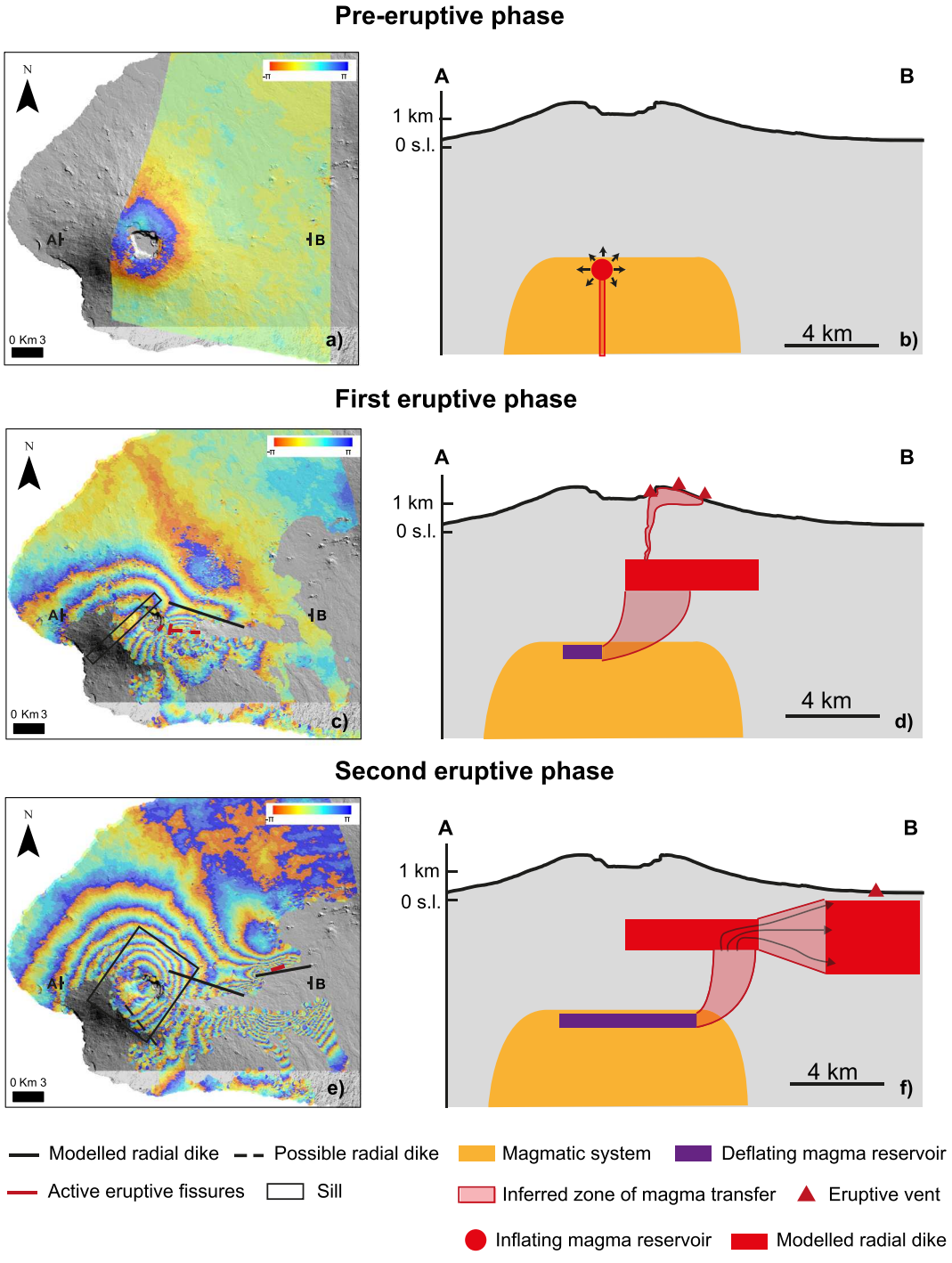

Figure 9. Conceptual model. Pre-eruptive deformation (a) due to new magma supply within the shallow magma reservoir of Cerro Azul (b). (c) Sin-eruptive deformation of the first eruptive phase related to the deflation of the shallow magma reservoir and the propagation of a proximal radial dike (d). (e) Deformation occurred during the second eruptive phase. Much more magma was supplied from the reservoir to a distal dike (f). Sections in b, d, and f are E-W trending, passing through the caldera.

volume lost by the sill and also to the volume of magma intruded in the previous 7 months (Tables 1 and 2). This suggests that the magma stored in the pre-eruptive period may have been remobilized during the first eruptive phase, promoting the subsidence of the magmatic reservoir and the emplacement of the radial dike. The geodetic signal associated with the opening of the eruptive fissures of the first phase is probably hidden

by that of the radial dike. One explanation is that the volume of magma involved in the eruptions at the summit vents during the first eruptive phase was negligible compared to that of the radial dike. This proposed scenario is similar to that inferred for the 1998 eruption at Cerro Azul (Teasdale et al., 2005), and agrees with the typical eruptive pattern of Cerro Azul, where the volume of lava erupted at the summit vents is usually much lower than that erupted along the lower flanks (Naumann & Geist, 2000). However, there are currently no estimates of the volume erupted during the two analyzed eruptive phases, and future studies should test this hypothesis.

The lower portion of the modeled dike is ~1.5 km shallower than the sill. We speculate that, from the northeast edge of the sill, an upward propagation of magma first occurred below the northeast sector of the caldera, which became a radial dike at shallower levels. The temporal resolution of our data does not allow us to test this hypothesis, as only the deformation associated to the radial dike is recorded. However, the inferred propagation pattern is similar to that observed in the last decades at Fernandina, where radial dikes generally initiate as sill-like intrusions that become progressively steeper below the caldera rim and twist around a radial horizontal axis (Bagnardi et al., 2013). The stress field imposed by the caldera unloading and the gravitational load of Cerro Azul may control this pattern of magma propagation, as at Fernandina (Corbi et al., 2015). The opening of the eruptive fissures of the first phase could have been related to a minor amount of magma that, during the initial steepening of the sill, propagated upward below the northeast caldera rim, reaching the surface. A limited lateral propagation of this dike may have fed the nearby fissures on the upper east flank.

On 1 June, the first eruptive phase ended, and the second phase began. This latter phase is associated with the eastward propagation of the radial dike of the first phase, which erupted (on 3 June) once it reached the topographic low coinciding with the plain between Cerro Azul and Sierra Negra. During this eruptive phase, the deflated area on the volcano summit became significantly larger, with the center of the subsidence migrating southeastward. We infer this to be due to the widening of the area of the magma reservoir from which the magma was withdrawn during this phase. The total volume lost by the magmatic system during this phase is about twice that lost during the first event. Some results suggest that the northern portion of the shallow magma reservoir, closer to the radial dike, lost a larger volume than the southern distal zone. Thus, the radial dike was fed mainly by the proximal area of the magmatic reservoir. Conversely, other results suggest that the subsidence on the southern flank may have been triggered by the propagation of a southeast oriented dike, probably during the second eruptive phase.

During this second phase, the estimated amount of magma of the radial dike is about twice the estimated volume lost by the magmatic reservoir and about five times greater than the volume that this dike had during the first phase. In addition, if the subsidence on the southern flank had been due to the propagation of another dike, the estimated volume of the dikes would become about three times greater than that lost by the magma reservoir. This suggests that an important magma supply from greater depth occurred at Cerro Azul between the first and the second eruptive phase; this may have promoted the further propagation of the eastern radial dike, triggering the eruption, the propagation of the southern dike, and the partial replenishment of the volume lost by the magma reservoir. An alternative explanation is an increase in the compressibility of the magma, which can account for volume discrepancy (Rivalta & Segall, 2008). In this context, during the first eruptive phase, the magma had to be nearly incompressible to explain the similarity in the volume lost by the reservoir and gained by the dike (Rivalta & Segall, 2008). During the second phase, the compressibility increased, for example, for an increase in the exsolved volatiles (Huppert & Woods, 2002), causing the apparent volume discrepancy. In any case, from the first to the second eruptive phase, there is an increase in the volume of magma supplied from the reservoir to the eastern radial dike, which could also have promoted the further propagation of the latter (Anderson & Poland, 2016).

From the first to the second eruptive phase, the eastern radial dike rotated anticlockwise by 28–33°, pointing toward Sierra Negra volcano, and stopped erupting in the depressed area between the two volcanoes. A similar change in the strike and arrest of a dike, when propagating from below a topographic high to a topographic low in front of a nearby volcanic edifice, was observed also during the 2014 Bardarbunga eruption (Sigmundsson et al., 2015). Topographic variation seems to be the main factor controlling this rotation and arrest between two nearby volcanoes (Heimisson et al., 2015; Sigmundsson et al., 2015; Urbani et al., 2017; Walter, 2003; Walter et al., 2006).

A new uplift within the caldera begun after the eruption; this continued in the following 3 years (Figures 3i–3k), characterized by nonconstant uplift rates.

7.1. Comparison Between Cerro Azul and the Other Western Galápagos Calderas

The deformation pattern of the caldera of Cerro Azul shows pre-eruptive uplift, coeruptive subsidence, and posteruptive uplift (Figures 3i–3k). This pattern is similar to that observed in other calderas of the western Galápagos, such as Fernandina in 2005 (Bagnardi & Amelung, 2012; Chadwick et al., 2011) and Sierra Negra in 2005 (Chadwick et al., 2006) and is typical of the mafic calderas (Acocella et al., 2015; Dvorak & Dzurisin, 1997).

Most of the deformation related to the 2008 eruption of Cerro Azul is caused by the propagation of a radial dike. This is typical of the western Galápagos volcanoes, where the eruptions along the flanks of these volcanoes are related to radial dikes (Chadwick & Dieterich, 1995). The propagation pattern of the radial dikes proposed for Fernandina (Bagnardi et al., 2013), where a sill-like intrusion progressively turns upward and twists around a horizontal radial axis, also seems applicable for the 2008 radial dike of Cerro Azul.

According to our results, the magma reservoir constantly fed the radial dike during the two eruptive phases, increasing the volume of magma transferred from the reservoir to the dike during the second eruptive phase. This situation is different to what happened at neighboring Alcedo volcano during the 2010 unrest, where the lack of new magma supply during unrest stopped an incipient lateral propagation of a sill (Galetto et al., 2019), confirming the importance of a continuous supply of magma in the propagation of a dike/sill.

Finally, GPS data show a decrease in the uplift rate of Sierra Negra during the 2008 eruption of Cerro Azul (Poland, 2014). This suggests a possible connection between the two nearby volcanoes at deeper levels, similar to what is observed at the Aira-Kirishima system (SW Japan; Brothelande et al., 2018). This possibility is reinforced by petrological data, which suggest a common source in the lithospheric mantle for the magmas of Cerro Azul and Sierra Negra (Naumann et al., 2002). The anticorrelation of deformation between Cerro Azul and Sierra Negra can be tested only in 2008, as no deformation data are available for other periods, with the exception of the 2005 eruption of Sierra Negra, when Cerro Azul apparently did not deform. Future studies should test this working hypothesis, to understand better the deep plumbing system of these two volcanoes and to try to correlate the dynamics of the deep plumbing system with that of the shallower plumbing system.

8. Conclusions

The unwrapping limitations affecting our ENVISAT data gave us the opportunity to test a new method, based on the wrapped phase differences among nearby pixels, to model the wrapped data directly. Thanks to this method, we successfully inverted the deformation data of the two eruptive phases of Cerro Azul, recorded by the ascending track data of ENVISAT. Results show that after 7 months of pre-eruptive uplift, an eruption, divided in two eruptive phases, occurred at Cerro Azul in 2008. During the first eruptive phase, the incipient propagation of a radial dike promoted uplift on the east flank of Cerro Azul and a coeval first episode of deflation below the caldera, related to its magma reservoir. Eruptions occurred in the upper east flank during the first eruptive phase. The further lateral propagation of the radial dike triggered the second eruptive phase. The radial dike changed its strike when it propagated from below the volcanic edifice to a topographic low, between Cerro Azul and Sierra Negra.

Acknowledgments
We thank the Associate Editor M. Poland, S. Jónsson, and an anonymous reviewer for the helpful suggestions, which improved the quality of this manuscript. The ENVISAT data are distributed by the European Space Agency (ESA) via ESA's Virtual Archive (http://eo-virtual-archive4.esa.int/) in the framework of the Geohazard Supersites and Natural Laboratory initiative. The ALOS-PALSAR data are copyright JAXA/METI. Landsat 7 image in Figure 1 is freely distributed by the USGS from https://earthexplorer.usgs.gov/ . The grant to the Department of Science, Roma Tre University (MIUR-Italy Dipartimenti di Eccellenza, ARTICOLO 1, COMMI 314–337 LEGGE 232/2016) is acknowledged. This work was part supported by the European EUROVOLC project (grant number 731070) and the NERC Centre for the Observation and Modelling of Earthquakes, Volcanoesand Tectonics (COMET). The supporting information tables and figures are available at https://osf.io/gzaxq/?view_only=bcd204c5082c4025af05ff378d316758.

References

Acocella, V., Di Lorenzo, R., Newhall, C., & Scandone, R. (2015). An overview of recent (1988 to 2014) caldera unrest: Knowledge and perspectives. *Reviews of Geophysics*, *53*, 896–955. https://doi.org/10.1002/2015RG000492

Amelung, F., Yun, S. H., Walter, T. R., Segall, P., & Kim, S. W. (2007). Stress control of deep rift intrusion at Mauna Loa Volcano, Hawaii. *Science*, *316*(5827), 1026–1030. https://doi.org/10.1126/science.1140035

Anderson, K. R., & Poland, M. P. (2016). Bayesian estimation of magma supply, storage, and eruption rates using a multiphysical volcano model: Kīlauea Volcano, 2000–2012. *Earth and Planetary Science Letters*, *447*, 161–171. https://doi.org/10.1016/j.epsl.2016.04.029

Bagnardi, M., & Amelung, F. (2012). Space-geodetic evidence for multiple magma reservoirs and subvolcanic lateral intrusions at Fernandina Volcano, Galápagos Islands. *Journal of Geophysical Research*, *117*, B10406. https://doi.org/10.1029/2012JB009465

Bagnardi, M., Amelung, F., & Poland, M. P. (2013). A new model for the growth of basaltic shields based on deformation of Fernandina volcano, Galápagos Islands. *Earth and Planetary Science Letters*, *377*, 358–366. https://doi.org/10.1016/j.epsl.2013.07.016

Bagnardi, M., & Hooper, A. (2018). Inversion of surface deformation data for rapid estimates of source parameters and uncertainties: A Bayesian approach. *Geochemistry, Geophysics, Geosystems*, *19*, 2194–2211. https://doi.org/10.1029/2018GC007585

Baker, S., & Amelung, F. (2012). Top-down inflation and deflation at the summit of Kīlauea Volcano, Hawai'i observed with InSAR. *Journal of Geophysical Research*, *117*, B12406. https://doi.org/10.1029/2011JB009123

Biggs, J., Ebmeier, S. K., Aspinall, W. P., Lu, Z., Pritchard, M. E., Sparks, R. S. J., & Mather, T. A. (2014). Global link between deformation and volcanic eruption quantified by satellite imagery. *Nature Communications*, *5*, 3471. https://doi.org/10.1038/ncomms4471

Biggs, J., Robertson, E., & Cashman, K. (2016). The lateral extent of volcanic interactions during unrest and eruption. *Nature Geoscience*, *9*(4), 308–311. https://doi.org/10.1038/ngeo2658

Brothelande, E., Amelung, F., Yunjun, Z., & Wdowinski, S. (2018). Geodetic evidence for interconnectivity between Aira and Kirishima magmatic systems, Japan. *Scientific reports*, *8*(1), 9811. https://doi.org/10.1038/s41598-018-28026-4

Chadwick, W. W. Jr., & Dieterich, J. H. (1995). Mechanical modeling of circumferential and radial dike intrusion on Galápagos volcanoes. *Journal of Volcanology and Geothermal Research*, *66*, 37–52. https://doi.org/10.1016/0377-0273(94)00060-T

Chadwick, W. W. Jr., Geist, D. J., Jónsson, S., Poland, M., Johnson, D. J., & Meertens, C. M. (2006). A volcano bursting at the seams: Inflation, faulting, and eruption at Sierra Negra volcano, Galápagos. *Geology*, *34*, 1025–1028. https://doi.org/10.1130/G22826A.1

Chadwick, W. W., & Howard, K. A. (1991). The pattern of circumferential and radial eruptive fissures on the volcanoes of Fernandina and Isabela islands, Galapagos. *Bulletin of Volcanology*, *53*, 259–275. https://doi.org/10.1007/BF00414523

Chadwick, W. W., Jónsson, S., Geist, D. J., Poland, M., Johnson, D. J., Batt, S., et al. (2011). The May 2005 eruption of Fernandina volcano, Galápagos: The first circumferential dike intrusion observed by GPS and InSAR. *Bulletin of Volcanology*, *73*(6), 679–697. https://doi.org/10.1007/s00445-010-0433-0

Corbi, F., Rivalta, E., Pinel, V., Maccaferri, F., & Acocella, V. (2016). Understanding the link between circumferential dikes and eruptive fissures around calderas based on numerical and analog models. *Geophysical Research Letters*, *43*, 6212–6219. https://doi.org/10.1002/2016GL068721

Corbi, F., Rivalta, E., Pinel, V., Maccaferri, F., Bagnardi, M., & Acocella, V. (2015). How caldera collapse shapes the shallow emplacement and transfer of magma in active volcanoes. *Earth and Planetary Science Letters*, *431*, 287–293. https://doi.org/10.1016/j.epsl.2015.09.028

Decriem, J., Árnadóttir, T., Hooper, A., Geirsson, H., Sigmundsson, F., Keiding, M., et al. (2010). The 2008 May 29 earthquake doublet in SW Iceland. *Geophysical Journal International*, *181*, 1128–1146. https://doi.org/10.1111/j.1365-246X.2010.04565.x

Duputel, Z., Agram, P. S., Simons, M., Minson, S. E., & Beck, J. L. (2014). Accounting for prediction uncertainty when inferring subsurface fault slip. *Geophysical Journal International*, *197*, 464–482. https://doi.org/10.1093/gji/ggt517

Dvorak, J. J., & Dzurisin, D. (1997). Volcano geodesy: The search for magma reservoirs and the formation of eruptive vents. *Reviews of Geophysics*, *35*, 343–384. https://doi.org/10.1029/97RG00070

Ebmeier, S. K., Biggs, J., Mather, T. A., & Amelung, F. (2013). Applicability of InSAR to tropical volcanoes: Insights from Central America. *Geological Society, London, Special Publications*, *380*, 15–37. https://doi.org/10.1144/SP380.2

Edmonds, M., Cashman, K. V., Holness, M., & Jackson, M. (2019). Architecture and dynamics of magma reservoirs. https://doi.org/10.1098/rsta.2018.0298

Farr, T. G., Rosen, P. A., Caro, E., Crippen, R., Duren, R., Hensley, S., et al. (2007). The shuttle radar topography mission. *Reviews of Geophysics*, *45*, RG2004. https://doi.org/10.1029/2005RG000183

Feighner, M. A., & Richards, M. A. (1994). Lithospheric structure and compensation mechanisms of the Galápagos Archipelago. *Journal of Geophysical Research*, *99*, 6711–6729. https://doi.org/10.1029/93JB03360

Gaddes, M. E., Hooper, A., & Bagnardi, M. (2019). Using machine learning to automatically detect volcanic unrest in a time series of interferograms. *Journal of Geophysical Research: Solid Earth*, *124*, 12,304–12,322. https://doi.org/10.1029/2019JB017519

Galetto, F., Bagnardi, M., Acocella, V., & Hooper, A. (2019). Noneruptive unrest at the caldera of Alcedo Volcano (Galápagos Islands) revealed by InSAR Data and Geodetic Modeling. *Journal of Geophysical Research: Solid Earth*, *124*, 3365–3381. https://doi.org/10.1029/2018JB017103

Geist, D., Diefenbach, B. A., Fornari, D. J., Kurz, M. D., Harpp, K., & Blusztajn, J. (2008). Construction of the Galápagos platform by large submarine volcanic terraces. *Geochemistry, Geophysics, Geosystems*, *9*, Q03015. https://doi.org/10.1029/2007GC001795

Geist, D. J., Bergantz, G., & Chadwick, W. W. Jr. (2014). Galápagos magma chambers. In K. S. Harpp, E. Mittelstaedt, N. d'Ozouville, & D. W. Graham (Eds.), *The Galápagos: A Natural Laboratory for the Earth Sciences*, (Vol. 204, pp. 55–70). Hoboken, NJ: John Wiley & Sons. https://doi.org/10.1002/9781118852538.ch5

Gibson, S. A., & Geist, D. (2010). Geochemical and geophysical estimates of lithospheric thickness variation beneath Galápagos. *Earth and Planetary Science Letters*, *300*, 275–286. https://doi.org/10.1016/j.epsl.2010.10.002

Global Volcanism Program (2008). Report on Cerro Azul (Ecuador). In R. Wunderman (Ed.), *Bulletin of the Global Volcanism Network* (Vol. 33, no. 5). Smithsonian Institution. https://doi.org/10.5479/si.GVP.BGVN200805-353060

González, P. J., Bagnardi, M., Hooper, A. J., Larsen, Y., Marinkovic, P., Samsonov, S. V., & Wright, T. J. (2015). The 2014–2015 eruption of Fogo volcano: Geodetic modeling of Sentinel-1 TOPS interferometry. *Geophysical Research Letters*, *42*, 9239–9246. https://doi.org/10.1002/2015GL066003

Hanssen, R. F. (2001). *Radar interferometry data interpretation and error analysis* (p. 328). New York: Springer. https://doi.org/10.1007/0-306-47633-9

Hanssen, R. F., Weckwerth, T. M., Zebker, H. A., & Klees, R. (1999). High-resolution water vapor mapping from interferometric radar measurements. *Science*, *283*(5406), 1297–1299. https://doi.org/10.1126/science.283.5406.1297

Harpp, K. S., & Geist, D. J. (2018). The evolution of Galápagos Volcanoes: An alternative prospective. *Frontiers in Earth Science*, *6*, 50. https://doi.org/10.3389/feart.2018.00050

Heimisson, E. R., Hooper, A., & Sigmundsson, F. (2015). Forecasting the path of a laterally propagating dike. *Journal of Geophysical Research: Solid Earth*, *120*, 8774–8792. https://doi.org/10.1002/2015JB012402

Hooft, E. E., Toomey, D. R., & Solomon, S. C. (2003). Anomalously thin transition zone beneath the Galápagos hotspot. *Earth and Planetary Science Letters*, *216*, 55–64. https://doi.org/10.1016/S0012-821X(03)00517-X

Hooper, A. (2008). A multi-temporal InSAR method incorporating both persistent scatterer and small baseline approaches. *Geophysical Research Letters*, *35*, L16302. https://doi.org/10.1029/2008GL034654

Hooper, A. (2010a). A statistical-cost approach to unwrapping the phase of InSAR time series. In Proceedings of the International Workshop on ERS SAR Interferometry, Frascati, Italy (Vol. 30).

Hooper, A. (2010b). Bayesian inversion of wrapped InSAR data for geophysical parameter estimation. In *ESA Living Planet Symposium*, 8 June to 2 July 2010 (ESA SP-686, December 2010, (Vol. 686). Bergen.

Hooper, A., Bekaert, D., Spaans, K., & Ankan, M. (2012). Recent advances in SAR interferometry time series analysis for measuring crustal deformations. *Tectonophysics*, *514*, 1–13. https://doi.org/10.1016/j.tecto.2011.10.013

Hooper, A., & Zebker, H. A. (2007). Phase unwrapping in three dimensions with application to InSAR time series. *Journal of the Optical Society of America*, *24*, 2737–2747. https://doi.org/10.1364/JOSAA.24.002737

Huppert, H. E., & Woods, A. W. (2002). The role of volatiles in magma chamber dynamics. *Nature*, *420*(6915), 493–495. https://doi.org/10.1038/nature01211

Jónsson, S. (2009). Stress interaction between magma accumulation and trapdoor faulting on Sierra Negra volcano, Galápagos. *Tectonophysics*, *471*, 36–44. https://doi.org/10.1016/j.tecto.2008.08.005

Just, D., & Bamler, R. (1994). Phase statistics of interferograms with applications to synthetic aperture radar. *Applied Optics*, *33*(20), 4361–4368. https://doi.org/10.1364/AO.33.004361

Kruskal, J. B. (1956). On the shortest spanning subtree of a graph and the traveling salesman problem. *Proceedings of the American Mathematical Society*, *7*, 48–50. https://www.jstor.org/stable/2033241

Mouginis-Mark, P. J., Snell, H., & Ellisor, R. (2000). GOES satellite and field observations of the 1998 eruption of Volcan Cerro Azul, Galapagos Islands. *Bulletin of Volcanology*, *62*(3), 188–198. https://doi.org/10.1007/s004450000078

Naumann, T., & Geist, D. (2000). Physical volcanology and structural development of Cerro Azul Volcano, Isabela Island, Galápagos: Implications for the development of Galápagos-type shield volcanoes. *Bulletin of Volcanology*, *61*(8), 497–514. https://doi.org/10.1007/s004450050001

Naumann, T., Geist, D., & Kurz, M. (2002). Petrology and geochemistry of Volcán Cerro Azul: Petrologic diversity among the western Galapagos volcanoes. *Journal of Petrology*, *43*, 859–883. https://doi.org/10.1093/petrology/43.5.859

Naumann, T. R., & Geist, D. J. (1999). Generation of alkalic basalt by crystal fractionation of tholeiitic magma. *Geology*, *27*, 423–426.

Newhall, C. G., Dzurisin, D. (1988) Historical unrest at large calderas of the world. (Vol. 2). U.S. Geol. Surv. Bull., 1855, 1108.

Nikkhoo, M., Walter, T. R., Lundgren, P. R., & Prats-Iraola, P. (2017). Compound dislocation models (CDMs) for volcano deformation analyses. *Geophysical Journal International*, *208*, 877–894. https://doi.org/10.1093/gji/ggw427

Okada, Y. (1985). Surface deformation due to shear and tensile faults in a half-space. *Bulletin of the seismological society of America*, *75*, 1135–1154.

Pinel, V., Poland, M. P., & Hooper, A. (2014). Volcanology: Lessons learned from synthetic aperture radar imagery. *Journal of Volcanology and Geothermal Research*, *289*, 81–113. https://doi.org/10.1016/j.jvolgeores.2014.10.010

Poland, M. P. (2014). Contrasting volcanism in Hawai'i and the Galápagos. In K. S. Harpp, E. Mittelstaedt, N. d'Ozouville, & D. W. Graham (Eds.), *The Galápagos: A Natural Laboratory for the Earth Sciences* (Vol. 204, pp. 5–26). Hoboken, NJ: John Wiley & Sons.

Poland, M. P., Lisowski, M., Dzurisin, D., Kramer, R., McLay, M., & Pauk, B. (2017). Volcano geodesy in the Cascade arc, USA. *Bulletin of Volcanology*, *79*(8), 1–33. https://doi.org/10.1007/s00445-017-1140-x

Prim, R. C. (1957). Shortest connection networks and some generalizations. *The Bell System Technical Journal*, *36*(6), 1389–1401. https://doi.org/10.1002/j.1538-7305.1957.tb01515.x

Rivalta, E., & Segall, P. (2008). Magma compressibility and the missing source for some dike intrusions. *Geophysical Research Letters*, *35*, L04306. https://doi.org/10.1029/2007GL032521

Rosen, P. A., Gurrola, E., Sacco, G. F., & Zebker, H. (2012). The InSAR scientific computing environment. In Synthetic Aperture Radar, 2012. EUSAR. 9th European Conference on, pp. 730-733. VDE.

Rowland, S. K., Harris, A. J., Wooster, M. J., Amelung, F., Garbeil, H., Wilson, L., & Mouginis-Mark, P. J. (2003). Volumetric characteristics of lava flows from interferometric radar and multispectral satellite data: The 1995 Fernandina and 1998 Cerro Azul eruptions in the western Galapagos. *Bulletin of Volcanology*, *65*(5), 311–330. https://doi.org/10.1007/s00445-002-0262-x

Rychert, C. A., Harmon, N., & Ebinger, C. (2014). Receiver function imaging of lithospheric structure and the onset of melting beneath the Galápagos Archipelago. *Earth and Planetary Science Letters*, *388*, 156–165. https://doi.org/10.1016/j.epsl.2013.11.027

Sandri, L., Acocella, V., & Newhall, C. (2017). Searching for patterns in caldera unrest. *Geochemistry, Geophysics, Geosystems*, *18*, 2748–2768 . https://doi.org/10.1002/2017GC006870

Sigmundsson, F., Hooper, A., Hreinsdóttir, S., Vogfjörd, K. S., Ófeigsson, B. G., Heimisson, E. R., et al. (2015). Segmented lateral dyke growth in a rifting event at Bárðarbunga volcanic system, Iceland. *Nature*, *517*(7533), 191–195. https://doi.org/10.1038/nature14111

Sparks, R. S. J., Annen, C., Blundy, J. D., Cashman, K. V., Rust, A. C., & Jackson, M. D. (2019). Formation and dynamics of magma reservoirs. *Philosophical Transactions of the Royal Society A*, *377*. https://doi.org/10.1098/rsta.2018.0019

Teasdale, R., Geist, D., Kurz, M., & Harpp, K. (2005). 1998 eruption at Volcán Cerro Azul, Galápagos Islands: I. Syn-Eruptive Petrogenesis. *Bulletin of Volcanology*, *67*(2), 170–185. https://doi.org/10.1007/s00445-004-0371-9

Urbani, S., Acocella, V., Rivalta, E., & Corbi, F. (2017). Propagation and arrest of dikes under topography: Models applied to the 2014 Bardarbunga (Iceland) rifting event. *Geophysical Research Letters*, *44*, 6692–6701. https://doi.org/10.1002/2017GL073130

Villagómez, D. R., Toomey, D. R., Geist, D. J., Hooft, E. E., & Solomon, S. C. (2014). Mantle flow and multistage melting beneath the Galápagos hotspot revealed by seismic imaging. *Nature Geoscience*, *7*(2), 151–156. https://doi.org/10.1038/NGEO2062

Walter, T. R. (2003). Buttressing and fractional spreading of Tenerife, an experimental approach on the formation of rift zones. *Geophysical Research Letters*, *30*(6), 1296. https://doi.org/10.1029/2002GL016610

Walter, T. R., Klügel, A., & Münn, S. (2006). Gravitational spreading and formation of new rift zones on overlapping volcanoes. *Terra Nova*, *18*, 26–33. https://doi.org/10.1111/j.1365-3121.2005.00656.x

White, W. M., McBirney, A. R., & Duncan, R. A. (1993). Petrology and geochemistry of the Galápagos Islands: Portrait of a pathological mantle plume. *Journal of Geophysical Research*, *98*, 19,533–19,563. https://doi.org/10.1029/93JB02018

Wright, T. J., Ebinger, C., Biggs, J., Ayele, A., Yirgu, G., Keir, D., & Stork, A. (2006). Magma-maintained rift segmentation at continental rupture in the 2005 Afar dyking episode. *Nature*, *442*(7100), 291–294. https://doi.org/10.1038/nature04978

Xu, W., Jónsson, S., Ruch, J., & Aoki, Y. (2016). The 2015 Wolf volcano (Galápagos) eruption studied using Sentinel-1 and ALOS-2 data. *Geophysical Research Letters*, *43*, 9573–9580. https://doi.org/10.1002/2016GL069820

Yun, S., Segall, P., & Zebker, H. (2006). Constraints on magma chamber geometry at Sierra Negra Volcano, Galápagos Islands, based on InSAR observations. *Journal of Volcanology and Geothermal Research*, *150*, 232–243. https://doi.org/10.1016/j.jvolgeores.2005.07.009

Yun, S. H., Zebker, H., Segall, P., Hooper, A., & Poland, M. (2007). Interferogram formation in the presence of complex and large deformation. *Geophysical Research Letters*, *34*, L12305. https://doi.org/10.1029/2007GL029745